

A global circulation model of Saturn's thermosphere

I.C.F. Müller-Wodarg^{a,*}, M. Mendillo^b, R.V. Yelle^c, A.D. Aylward^d

^a *Space and Atmospheric Physics Group, Imperial College, London, UK*

^b *Center for Space Physics, Boston University, Boston, MA 02215, USA*

^c *Lunar and Planetary Laboratory, Tucson, AZ 85721, USA*

^d *Atmospheric Physics Laboratory, University College, London, UK*

Received 6 May 2004; revised 1 September 2005

Available online 10 November 2005

Abstract

We present the first 3-dimensional self-consistent calculations of the response of Saturn's global thermosphere to different sources of external heating, giving local time and latitudinal changes of temperatures, winds and composition at equinox and solstice. Our calculations confirm the well-known finding that solar EUV heating alone is insufficient to produce Saturn's observed low latitude thermospheric temperatures of 420 K. We therefore carry out a sensitivity study to investigate the thermosphere's response to two additional external sources of energy, (1) auroral Joule heating and (2) empirical wave heating in the lower thermosphere. Solar EUV heating alone produces horizontal temperature variations of below 20 K, which drive horizontal winds of less than 20 m/s and negligible horizontal changes in composition. In contrast, Joule heating produces a strong dynamical response with westward winds comparable to the sound speed on Saturn. Joule heating alone, at a total rate of 9.8 TW, raises polar temperatures to around 1200 K, but values equatorward of 30° latitude, where observations were made, remain below 200 K due to inefficient meridional energy transport in a fast rotating atmosphere. The primarily zonal wind flow driven by strong Coriolis forces implies that energy from high latitudes is transported equatorward mainly by vertical winds through adiabatic processes, and an additional 0.29–0.44 mW/m² thermal energy are needed at low latitudes to obtain the observed temperature values. Strong upwelling increases the H₂ abundances at high latitudes, which in turn affects the H₃⁺ densities. Downwelling at low latitudes helps increase atomic hydrogen abundances there.

© 2005 Elsevier Inc. All rights reserved.

Keywords: Saturn; Thermosphere; Joule heating; Winds; Temperatures; General Circulation Model

1. Introduction

Most of our current knowledge about Saturn's atmosphere originates from the two Voyager missions in 1980 and 1981. The radio occultation experiment provided temperature values for the troposphere and stratosphere (Lindal et al., 1985; Lindal, 1992), while remote sensing measurements of thermospheric temperatures were provided by the solar and stellar occultation experiments with the ultraviolet spectrometer (UVS) (Festou and Atreya, 1982; Smith et al., 1983). These measurements placed Saturn's thermosphere above the 100 nbar level (located around 800 km above the 1 bar level). Some ambiguity remains regarding the value of non-auroral exospheric temperature on Saturn since two very different values were derived from the

Voyager data. From the solar occultation experiment a value of ~420 K near 30° N latitude was derived for altitudes above 1500 km (Smith et al., 1983), while the stellar occultation experiment at 4° N latitude suggested a value of ~800 K (Festou and Atreya, 1982). A comparative discussion of these results was presented by Smith and Hunten (1990). For the current study we adopt the lower temperature measurement of ~420 K. No information about the mesosphere could be inferred from the Voyager data, but results from ground based observations of the stellar occultation of 28 Sgr in 1986 suggested virtually constant temperatures there with a value of 141 K between 1 mbar and 0.3 μbar (Hubbard et al., 1997). Their measurements also extended into the lower thermosphere, near 50 nbar.

The principal gases in Saturn's thermosphere above the homopause are H₂, H, He and, near the homopause, CH₄. Values of their mixing ratios were first inferred from the solar and stellar occultation observations by Voyager's UVS instrument

* Corresponding author.

E-mail address: i.mueller-wodarg@imperial.ac.uk (I.C.F. Müller-Wodarg).

(Festou and Atreya, 1982; Smith et al., 1983). Hydrocarbons near the homopause act as coolants by releasing the energy conducted down from the thermosphere as infrared radiation. The altitude of Saturn's homopause is still subject to debate, with some studies suggesting it to lie within the lower thermosphere, while others have placed it at the bottom of the thermosphere.

The most recent comprehensive 1-dimensional calculations of chemistry in Saturn's neutral atmosphere were presented by Moses et al. (2000a, 2000b) and Ollivier et al. (2000). These models concentrated on the complex hydrocarbon photochemistry of Saturn's stratosphere, but extended into the thermosphere as well, where photochemistry is far less complex than below the homopause. These models did not calculate the thermal structure of Saturn's atmosphere, but assumed a fixed temperature profile inferred from Voyager, Infrared Space Observatory (ISO) and other observations. To date, no calculations of Saturn's thermal structure have been published.

In order to gain a better understanding of the global distribution of temperatures, composition and winds, General Circulation Models (GCMs) have for the past decades been applied very successfully to upper atmospheres of all terrestrial planets (Roble et al., 1988; Fuller-Rowell et al., 1996; Bougher et al., 1999, 2000, 2002), Jupiter (Achilleos et al., 1998; Millward et al., 2002; Bougher et al., 2005), Titan (Müller-Wodarg et al., 2000, 2003) and Triton (Müller-Wodarg, 2002). They numerically solve the global time-dependent non-linear coupled equations of continuity, momentum and energy, allowing the diagnosis of the morphology of complex atmospheric processes, including global dynamics. General Circulation Models prove to be invaluable tools for understanding the 3-dimensional time-dependent behavior of planetary atmospheres.

In this study, we present the first application of a GCM to the thermosphere of Saturn. Our goal is to assess, through sensitivity studies, the range of responses of Saturn's upper atmosphere to different sources of energy. We will present the global temperatures and dynamics resulting from solar EUV heating alone and those resulting from high latitude Joule heating and global wave heating.

Our model forms the basis for a fully coupled Saturn Thermosphere–Ionosphere Model (STIM) which is in advanced stages of development and will ultimately allow us to study Saturn's global ionosphere and its chemical, energetic and dynamical coupling to the thermosphere and magnetosphere. The STIM–GCM will be built up of several coupled modules, each calculating specific physical regimes of Saturn's upper atmosphere. First results of the STIM ionosphere module appeared in Moore et al. (2004) and Mendillo et al. (2005) and for Saturn's inner plasmasphere in Moore and Mendillo (2005). More comprehensive simulations examining Saturn's global response to Joule heating, using the same thermosphere model as this study, are presented by Smith et al. (2005a).

Section 2 discusses energetics of Saturn's upper atmosphere, Section 3 will introduce basic properties of our model (with more detailed information given in Appendix A). In Section 4 we describe our simulations and examine implications and consequences of the assumptions made. Section 5 discusses horizontal structures in temperatures and composition as well as

global circulation for different conditions on Saturn. Section 6 gives concluding comments and discusses any limitations of our approach.

2. Energetics of Jupiter's and Saturn's thermospheres

All Gas Giants, including Saturn, have been found to possess exospheric temperatures which exceed by factors of ~ 2.5 (Saturn) to ~ 4.5 (Jupiter, Neptune) and ~ 5.8 (Uranus) the values expected on the basis of solar EUV heating only (Yelle and Miller, 2004). To date, it is unresolved what causes the high exospheric temperatures on Gas Giants. Possible mechanisms include (1) transport of energy from the lower into the upper atmosphere by upward propagating waves which dissipate in the thermosphere and (2) flow of energy from the magnetosphere and solar wind into the thermosphere/ionosphere system via auroral coupling processes such as particle precipitation and Joule heating, and transport of this energy across the planet. While further external energy sources have been proposed, the above are the most likely candidates. On Saturn both processes may play a role, but no observational evidence is yet available to determine their relative importance. Since more observational evidence is available for Jupiter, we will briefly review what is known about this planet and then attempt to draw parallels with Saturn.

A discussion of thermospheric heating on Jupiter was first presented by Strobel and Smith (1973). Assuming a 50% efficiency in the absorption of solar EUV radiation by H and H₂, as suggested by Waite et al. (1983), one can calculate the solar EUV heating rates for Jupiter and thereby the total solar EUV energy deposited into Jupiter's upper atmosphere. The calculated height-integrated EUV heating rate for Jupiter's thermosphere is around 0.02 mW/m² (globally averaged), depositing around 1.2 TW of solar EUV energy. When assuming that all energy is lost by vertical conduction downward, it is possible to estimate the expected exospheric temperature resulting from this EUV heating rate, using a simple equation presented by Hunten and Dessler (1977). Using this expression and the above solar EUV heating rates, Yelle and Miller (2004) derived a value of $T_{\text{exo}} \sim 203$ K, which is far smaller than the measured non-auroral value of 800–1000 K (Marten et al., 1994; Yelle et al., 1996; Yelle and Miller, 2004). In order to reproduce the vertical temperature gradients in Jupiter's lower thermosphere of around 3–10 K/km, Yelle et al. (1996) derived a necessary heating rate of around 1 mW/m² which, if applied globally, would translate into an energy input of around 65 TW. Recent observations of Jupiter's auroral brightness in the UV (Clarke et al., 2005) suggested heating rates due to particle precipitation of a few tens of TW, with Joule heating rates probably larger by a factor of 2–3, so total magnetospheric heating on Jupiter is on average a few ten times larger than solar EUV heating and could hence play a major role in generating the high exospheric temperatures, at least at high latitudes.

The possibility of gravity wave heating on Jupiter was first discussed by French and Gierasch (1974) and examined for the Galileo probe Atmospheric Structure Instrument (ASI) data by Young et al. (1997) and Matcheva and Strobel (1999) and re-

viewed by Yelle and Miller (2004). An approximate derived heating rate for the gravity waves detected by the Galileo probe is 0.4 mW/m^2 . If this rate applied globally, it would deposit around 26 TW of energy in the atmosphere. This figure can only be seen as a rough guess since no constraints are currently available to characterize the horizontal distribution of gravity waves and hence heating associated with them. However, gravity waves potentially have heating rates comparable to the magnetospheric ones, but act also at equatorial latitudes, where the ASI measurements were made. Gravity waves thus avoid the problem of energy transport from polar to equatorial latitudes posed by magnetospheric heating. Recently, Schubert et al. (2003) proposed acoustic waves as a further source of energy on Jupiter.

Another potential energy source proposed for Jupiter's and also Saturn's upper atmospheres is linked to the discovery of non-auroral X-ray emissions. Their origin has been subject to debate, with Waite et al. (1997) suggesting they could be generated by particle precipitation which heats Jupiter's thermosphere at a rate of 0.2 mW/m^2 . More recent observations indicate that the X-ray emissions are of solar origin and scattered off the atmospheres of Jupiter and Saturn (Maurellis et al., 2000; Bhardwaj et al., 2004, 2005). The low albedos (5×10^{-5}) which Bhardwaj et al. (2004) calculated for Jupiter suggested that an important part of the solar X-rays is absorbed in the scattering process, so they may provide an additional important source of energy. Investigating this in detail is beyond the scope of this paper.

Only few observations are available to constrain the energetics of Saturn's upper atmosphere. Assuming the same heating efficiencies as for Jupiter, we obtain globally averaged solar EUV heating rates of around 0.01 mW/m^2 (0.0046 mW/m^2) for solar maximum (minimum) conditions, which deposit a total of 0.27 TW (0.15 TW) into Saturn's upper atmosphere, insufficient to reproduce the observed exospheric temperatures.

We will therefore examine alternative thermal energy sources for Saturn and, drawing the parallel with Jupiter, we will in particular consider heating by waves and magnetospheric sources. Magnetospheric energy is available either through precipitating particles or Pedersen currents. The latter are driven by transfer of momentum between different plasma regions, either through solar-wind-magnetosphere interaction (as on Earth) or by radial transport of plasma originating from surfaces of moons inside the magnetosphere, as on Jupiter, or additional plasma from sputtered ring material, as on Saturn. Departure of magnetospheric plasma from corotation gives rise to field-perpendicular electric fields, which drive ionospheric Pedersen currents. These Pedersen currents cause Joule heating in Saturn's upper atmosphere. Recently, Cowley et al. (2004), assuming a height-integrated Pedersen conductivity of 1 mho, estimated total Joule heating rates for Saturn's thermosphere of $\sim 9.6 \text{ TW}$ (over both hemispheres), or a rate at high latitudes of up to $\sim 12\text{--}15 \text{ mW/m}^2$. A further contribution to magnetospheric energy input comes from precipitating particles, although this is probably second order to Joule heating. Observed auroral UV brightnesses, which are driven by par-

ticle precipitation, on Saturn are around 1–100 kR, fainter by an average factor of 100 than those of Jupiter (10–1000 kR) (Clarke et al., 2005).

We saw for the case of Jupiter that gravity waves could potentially deposit $\approx 0.4 \text{ mW/m}^2$ of energy in its upper atmosphere, which on Saturn would translate into $\approx 18 \text{ TW}$. It is therefore conceivable that Saturn's thermospheric temperatures are supported by wave heating alone or, more likely, a combination of wave heating and magnetospheric heating. The important question with magnetospheric heating is whether this energy could be transported equatorward by thermospheric dynamics. This is one of the questions we will be examining in this study. Both alternative energy sources would generate very different thermospheric dynamics, the magnetospheric heating driving strong winds at mid to high latitudes, whereas waves would drive circulation in the equatorial and low latitude regions. Since observations cannot currently constrain either of the cases, we present both and hence explore the possible parameter space for thermal structure and thermospheric dynamics with our model.

3. The model

Our Saturn thermosphere GCM solves globally the coupled non-linear Navier–Stokes equations of energy, momentum and continuity by explicit time integration. The model reaches from 100 nbar (800 km above the 1 bar level) to around 1×10^{-4} nbar ($\sim 3400 \text{ km}$ in a 420 K thermosphere). The model calculates in a physically self-consistent manner the response of Saturn's thermosphere to external energy sources, such as the build-up of temperatures and pressures on the dayside due to solar EUV heating and resulting horizontal and vertical winds. We consider all relevant processes of internal energy redistribution, such as molecular conduction, adiabatic heating and cooling, and horizontal and vertical advection. The calculations of winds consider pressure gradients, viscosity, Coriolis forces, curvature and momentum advection. We include the main gases H_2 , H and He and calculate their transport by winds and molecular and eddy diffusion. The basic set of ion–neutral photochemistry reactions is also included, as described by Moore et al. (2004), but ionospheric calculations will not be discussed as part of this study.

Initial neutral composition profiles are taken from Moses and Bass (2000). Fig. 1 shows a vertical profile of globally averaged gas mixing ratios throughout the model domain, illustrating that H_2 is the principal gas throughout most of Saturn's thermosphere and replaced by H only above 1×10^{-4} nbar. While the absorption of solar EUV radiation by each of the atmospheric gases is treated rigorously, we currently do not calculate the detailed energetics associated with the photochemistry and instead assume a heating efficiency of 50% for each absorbed photon, in agreement with estimates for Jupiter by Waite et al. (1983). Horizontal and vertical resolution are entirely flexible. In our simulations we used vertical spacing of 0.25 scale heights and horizontal resolution of 10° longitude times $2\text{--}6^\circ$ latitude (depending on the simulation), the time integration step is between 1 and 40 s. The full set of equations,

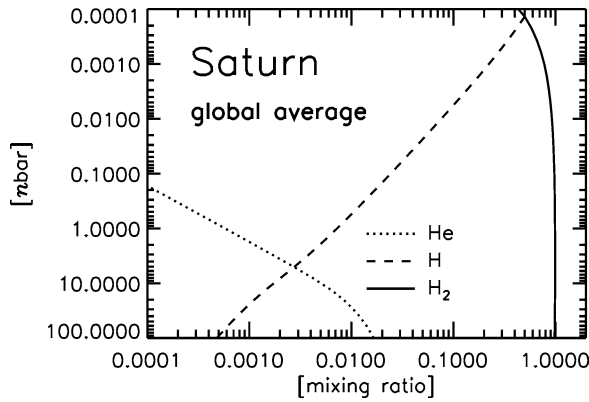


Fig. 1. Globally averaged mixing ratios of principal gases in Saturn's thermosphere. Values are consistent with Moses and Bass (2000).

boundary conditions and parameters of the model is given in Appendix A.

4. Simulations

In our study we have run the model for a number of seasonal conditions and external energy sources. Our simulations are summarized in Table 1. In each simulation we have run the model for 400 Saturn rotations in order to approach steady state, during which the solar declination angle was kept constant. Each run was started up using globally uniform vertical composition profiles taken from calculations by Moses et al. (2000a) and a globally uniform vertical temperature profile of 143 K. This was to ensure that any horizontal and vertical structures were due entirely to processes originating from within the GCM.

4.1. Solar EUV heating input

Simulations 1 and 2 (designated S1 and S2) are for conditions of solar minimum and maximum, respectively. In all runs we implemented fluxes from the SOLAR 2000 model in its latest version (2.24) (Tobiska et al., 2000; Tobiska, 2004). For solar minimum we averaged fluxes from September 14–27, 1996, and for solar maximum we averaged fluxes from January 1–14, 1990, periods with average F10.7 solar flux being 70 and

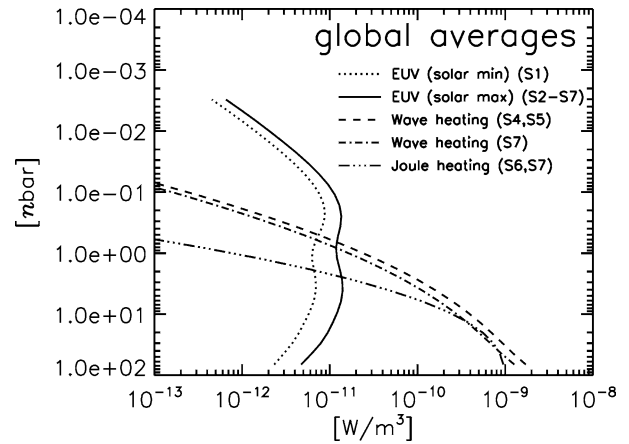


Fig. 2. Height profiles of globally averaged heating rates used in our simulations (denoted S1–S7). Solar EUV volume heating rates are given for solar maximum (solid) and minimum (dotted) conditions. Also shown are empirical wave heating rates (dashed and dashed–dotted) as well as Joule heating rates (dashed–triple dotted). See Table 1 and text for details.

180, respectively. All simulations except for S1 assume solar maximum conditions. As shown in Table 1, the resulting total solar EUV heating rates for solar minimum and maximum conditions respectively are 0.15 and 0.27 TW. The factor of 1.8 solar cycle effect is comparable to the factor of 2.3 variation of total solar energy across the EUV and FUV spectrum (7.5–103.2 nm) from solar minimum to solar maximum.

Vertical profiles of globally averaged volume heating rates are shown in Fig. 2 (solid and dotted lines). They exhibit a double-peak structure, maximizing near 0.3 and 4 nbar. The upper peak is due primarily to absorption by H₂ between 100 and 105 nm, the lower peak is due to absorptions below 35 nm, primarily by H₂ and H. These absorptions lead primarily to ionization, particularly in the He II line (30.38 nm). For a more comprehensive discussion of ionization rates, see Moore et al. (2004) and Moses and Bass (2000).

4.2. Wave heating input

In simulations S4, S5 and S7 we imposed empirical profiles of additional heating, which in the following we will refer to as “wave heating.” Since no measurements are currently available

Table 1
Summary of Saturn GCM simulations carried out for this study

| | Season | EUV heating (TW) | Joule heating (TW) | Wave heating (TW) |
|-------------------|----------|------------------|--------------------|-------------------|
| Simulation 1 (S1) | Equinox | 0.15 | 0 | 0 |
| Simulation 2 (S2) | Equinox | 0.27 | 0 | 0 |
| Simulation 3 (S3) | Solstice | 0.27 | 0 | 0 |
| Simulation 4 (S4) | Equinox | 0.27 | 0 | 14.0 ^a |
| Simulation 5 (S5) | Solstice | 0.27 | 0 | 14.0 ^a |
| Simulation 6 (S6) | Equinox | 0.27 | 9.82 | 0 |
| Simulation 7 (S7) | Equinox | 0.27 | 9.82 | 11.0 ^b |

^a “Solstice” refers to southern hemisphere summer conditions. Solar EUV heating rates assume 50% heating efficiencies and solar EUV fluxes from the SOLAR 2000 model (version 2.24) averaged over periods September 14–27, 1996 (solar minimum) and January 1–14, 1990 (solar maximum). Wave and Joule heating rates are discussed in Sections 4.2 and 4.3.

^a Wave heating applied globally uniform.

^b Wave heating with latitudinal structure shown in Fig. 3.

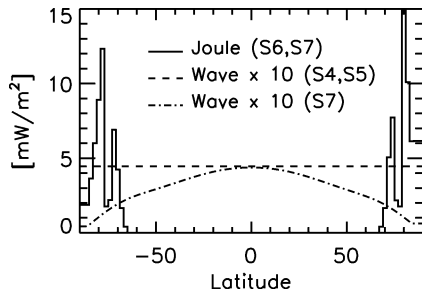


Fig. 3. Latitudinal profile of height integrated Joule heating rates (solid line) consistent with those proposed by Cowley et al. (2004), mapped onto our 2° resolution grid. Dashed and dashed–dotted lines are empirical wave heating rates (multiplied by 10) which we applied to match observed temperatures at low latitudes.

to determine whether waves on Saturn can produce these, our only justification for calling this “wave heating” is the similarity of these rates to those inferred for Jupiter (see discussion in Section 2). Our approach in determining this additional heating rate was to ask the question “*What additional energy is needed to obtain the observed exospheric temperatures?*” Two free parameters are present, namely, the latitude structure and altitude structure (in particular the altitude of peak heating).

In simulations S4 and S5 our aim was to generally raise the exospheric temperatures to observed levels without artificially introducing any horizontal structures. To achieve this, we implemented a latitudinally uniform wave heating profile, shown in Figs. 2 and 3 (dashed lines). The required heating rate was found to be 0.45 mW/m^2 , or 14.0 TW globally. This heating was assumed constant with local time and longitude.

In principle, the higher up in the atmosphere the energy is deposited, the lower the required rate to obtain the same exospheric temperatures. For upward propagating waves, the altitude at which they deposit any thermal energy depends on their vertical wavelengths, an unknown quantity. In our present simulations we assumed the peak wave heating to occur at our lower boundary, 100 nbar , using a Gaussian shape with 100 km mean half width, as shown in Fig. 2 (dashed and dashed–dotted curves). The derived heating rates can thus be regarded as upper limits to rates in the real atmosphere.

4.3. Joule heating input

In simulations S6 and S7 we applied Joule heating rates consistent with those proposed by Cowley et al. (2004). The latitudinal profiles of column integrated Joule heating rates used in our simulations are shown in Fig. 3 (solid line) versus latitude. For simplicity we assumed these to be constant with longitude and local time. Recent UV images of Saturn’s aurora show asymmetries with longitude and local time (Clarke et al., 2005), but implementing those will be subject of future studies. Due to the fine latitudinal structures of these profiles we used a latitudinal resolution of 2° in simulations S6 and S7 (as opposed to 6° in the others). Peak heating rates are $\approx 15 \text{ mW/m}^2$ near 80° N and $\approx 12 \text{ mW/m}^2$ near 78° S , and hence slightly asymmetric in both hemispheres. The asymmetries between north and south are due to the quadrupole terms in the Sat-

urn Pioneer Voyager (SPV) model of internal magnetic field (Davis and Smith, 1990), which results in north–south differences of the magnetic field strength, affecting the Joule heating rates. While the northern peak rate is larger, the region is wider in the south, and total heating rates are 4.86 TW in the north and 4.96 TW in the south, hence larger by 2% in the southern hemisphere. The total Joule heating rate we applied is hence 9.82 TW , slightly larger than the value by Cowley et al. (2004) due to the coarser latitude resolution in the model, but by an insignificant amount.

The vertical distribution of Joule heating implemented in S6 and S7 is shown in Fig. 2 (dashed–triple dotted line). We currently do not self-consistently calculate this profile, but impose it. Joule heating results from heating by collisions between plasma in Pedersen currents and the neutral atmosphere. The heating rate is thus strongest where the optimal balance occurs between ambient neutral densities and current density. This optimum situation is expected to occur in Gas Giant atmospheres around 1 scale height above the homopause (J. Clarke, personal communication, 2004). We placed the homopause at the lower boundary of our model since currently the complex hydrocarbon chemistry is not included, preventing us to extend our calculations below the homopause, where hydrocarbon abundances are expected to be significant. We hence imposed the peak of our volume Joule heating rate to be 1 scale height above our lower boundary, at 37 nbar . A Gaussian height profile centered around this peak is assumed, with a mean half width of 1 scale height, as shown in Fig. 2 (dashed–triple dotted line). A parallel study by Smith et al. (2005a), using the same model as here, investigates the dependence of Saturn’s thermospheric temperatures on the altitude and imposed rates of Joule heating.

For simplicity we ignore effects of ion drag, which is likely to accompany Joule heating. The horizontal convection electric fields formed in the magnetosphere are mapped into the high latitudes and accelerate the plasma there, which in turn collides with the ambient neutral gas and accelerates it. Our simplification is reasonable within the goals of this study. Recent ground-based observations by Stallard et al. (2004) detected line-of-sight H_3^+ velocities at roughly $1/3$ of Saturn’s corotation speed and indicated strong horizontal structures in the high latitude plasma velocities. At low latitudes, ion drag is likely to slow down the neutral velocities to some extent. We will introduce self-consistent calculations of ion drag in future versions of the STIM model, once we have more accurate information about the convection electric fields.

4.4. Multiple energy sources

In simulation S7 we added wave heating to given Joule heating (see Section 4.3), and in doing so we additionally introduced latitudinal structure in our wave heating profile, as shown in Fig. 3 (dashed–dotted curve). This adds little to the auroral latitudes, but “fills in” the low latitudes, where we compare to observed temperatures. By having a peak wave heating at the equator we also introduce an equator-to-pole pressure gradient, which will affect the dynamics. Our heating rates equatorward

of $\pm 50^\circ$ latitude range from 0.29 to 0.44 mW/m², the total wave energy input in S7 is 11.0 TW (see Table 1). These rates are comparable in magnitude to wave heating rates inferred for Jupiter by the Galileo probe observations (Young et al., 1997; Matcheva and Strobel, 1999; Yelle and Miller, 2004).

One aspect related to dissipating or breaking waves is the deposition of momentum into the background atmosphere. In the absence of any more detailed information we ignore this issue in our current study. If present, this would affect dynamics in the lower thermosphere. A more careful inclusion of momentum deposition associated with waves should be addressed in future studies, when more information is available about the wave properties.

5. Results

5.1. Thermal structure

Fig. 4 shows vertical profiles of temperatures from our simulations, averaged diurnally and between $\pm 30^\circ$ latitude. This range was chosen for easier comparison with observations, two of which are shown in the figure. Diamonds show the temperatures derived by Smith et al. (1983) from the Voyager EUV occultations, while crosses denote the upper range of temperatures derived by Hubbard et al. (1997) from the ground based 28 Sgr occultation measurements. While the two agree reasonably well near the 10-nbar level, they are different at lower altitudes.

We plotted the vertical temperature profiles only for simulations that differed notably. Not shown explicitly are S3, which is almost identical to S2, and S5, which closely resembles S4. Common in all simulations is the lower boundary temperature value of 143 K. As expected, we see clearly that temperatures in simulations S1, S2 and S3 are far smaller than the observed values, reaching merely 153 K (S1) and 160 K (S2, S3).

How sensitive are these values to our assumptions of heating efficiencies? When raising the EUV heating efficiencies from 50 to 100% in our model we increased exospheric temperatures at solar minimum by 13 K and at solar maximum by 25 K. It is clear from these experiments that solar energy absorbed by the

thermosphere even under the most favorable (and unrealistic) condition of 100% heating efficiencies is insufficient to raise temperatures in Saturn's thermosphere to observed levels.

In simulations S4 and S5 we implemented additional empirical wave heating (see Section 4.2) in order to obtain the observer exospheric temperatures, and the dashed–triple dotted curve in Fig. 4 hence closely matches the observed values above 1 nbar. Interestingly, the structure at lower altitudes differs from observations. This may be due to two reasons, our choice of height distribution of this empirical wave heating or, secondly, the absence of hydrocarbon photochemistry in the lower thermosphere of our model, which would generate infrared cooling, affecting the modeled temperature gradients.

In simulation S6 we ran the model with solar EUV and Joule heating (see Section 4.3). The important question here was whether the high latitude energy source could be distributed globally by winds and raise temperatures at low latitudes to observed values. We see that the temperatures we obtain reach around 187 K (dashed–dotted curve in Fig. 4), falling short of the observed values. This suggests that the Joule heating rates proposed by Cowley et al. (2004) are insufficient to explain the low latitude observations and that other heating sources are necessary. One of the main reasons for the ineffective redistribution of energy from higher towards lower latitudes is the planet's fast rotation, which causes substantial Coriolis forces to act, driving primarily zonal winds, as discussed further in Section 5.3. In simulation S7 we therefore added empirical wave heating to solar EUV and Joule heating in order to raise low latitude temperatures, so the profile (solid curve in Fig. 4) closely matches observations at altitudes above the 0.1-nbar level.

Investigation of the heating terms in our simulations (not shown) reveals that the external energy sources are balanced overwhelmingly by vertical heat conduction out of the bottom of the thermosphere. In runs S6 and S7, where wind speeds are considerable (see Section 5.3), internal energy redistribution processes become significant as well, such as adiabatic heating and cooling as well as advection. This will be further discussed in Section 5.4.

5.2. Solar driven dynamics

Fig. 5 shows latitude–local time profiles of temperatures and horizontal winds near the top of the thermosphere, at 3×10^{-3} nbar, from simulations S4 (panel (a)) and S5 (panel (b)). In these runs, the exospheric temperatures were raised by empirical wave heating which was implemented as a globally uniform source, hence adding no artificial horizontal variability. The horizontal structures in Fig. 5 are therefore driven entirely by changes in solar zenith angle. The purpose of investigating these is to determine diurnal and seasonal temperature changes and winds due to solar EUV heating. As shown previously, solar EUV energy is only a minor fraction of the energy flowing into the atmosphere in these simulations, so we would expect solar driven horizontal structures to be small.

Panel (a) in Fig. 5 shows the equinox case, where temperatures are largest over the equator. Diurnal variations are barely 2 K, equator-to-pole changes are twice that (4 K). The poleward

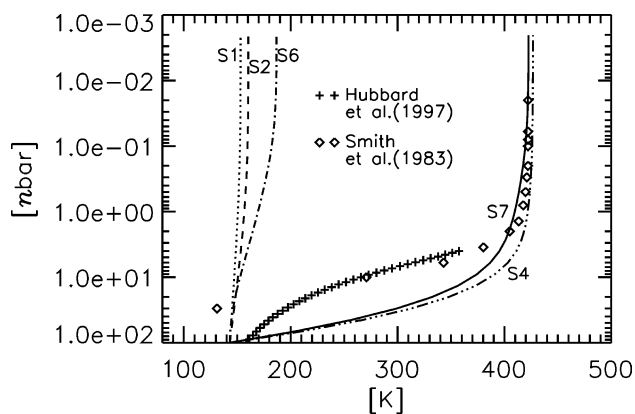


Fig. 4. Vertical profiles of temperatures averaged diurnally and over latitudes 30° S– 30° N, as calculated by the Saturn GCM (lines) in various simulations of this study (see also Table 1). Also shown are observations by Smith et al. (1983) (diamonds) and Hubbard et al. (1997) (crosses).

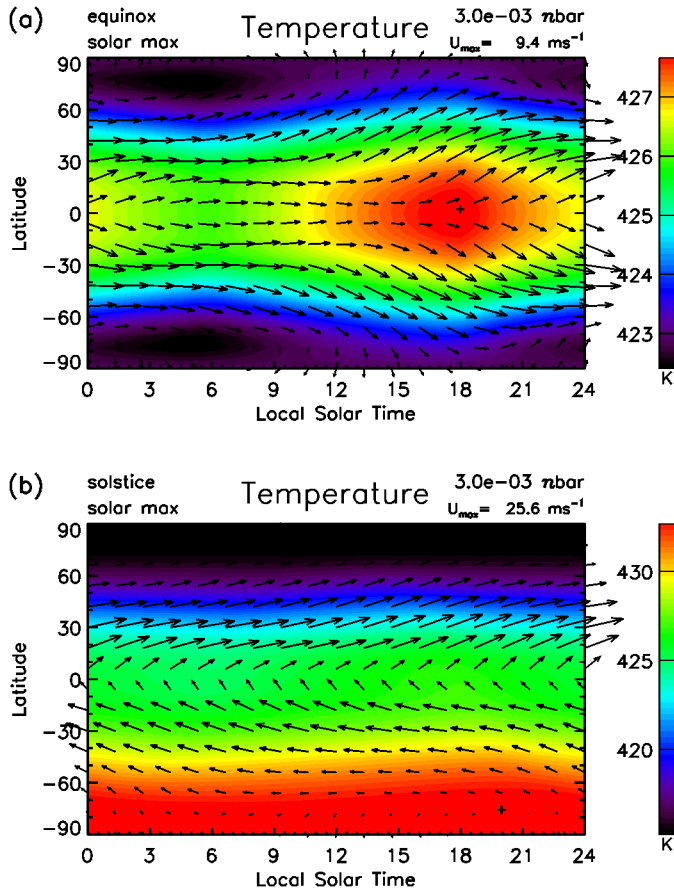


Fig. 5. Latitude–local time profiles of temperatures and horizontal winds at equinox conditions (panel (a)) and southern summer conditions (panel (b)) during solar maximum in Saturn’s upper thermosphere on the 3.0×10^{-3} nbar pressure level, as calculated by the GCM in simulations S4 and S5.

temperature (and pressure-) gradients drive poleward winds, which however are turned into eastward (corotating) winds by Coriolis forces, peaking at mid-latitudes with values of around 9 m/s. The temperature maximum occurs not at the subsolar point (noon), but at dusk (18 h local solar time). This is due to the large heat capacity of Saturn’s hydrogen/helium atmosphere ($c_p \approx 15,000$ J/kg/K) and hence long thermal time scale, combined with the fast rotation of the planet. Similarly, these two properties are partly responsible for the low diurnal variability of temperatures, and hence small horizontal and vertical winds.

At solstice (panel (b)), the hemispheric differences in temperature reach 16 K and hence dominate the diurnal variability, which is hardly visible in the contours of panel (b) (although still present). We show a case of southern hemisphere summer, as currently prevails on Saturn, so southern hemisphere temperatures are larger (432 K) than those in the north (416 K), driving a summer-to-winter pressure gradient, which itself drives meridional winds. These, however, are again turned into zonal winds by the strong Coriolis forces, westward in the southern (summer) hemisphere and eastward in the northern (winter) hemisphere, with peak velocities again occurring at mid-latitudes with values of up to 25 m/s, more than twice those found for equinox. Interestingly, the largest temperatures are found not at the subsolar latitude (26° S), but at the sum-

mer pole. This is the region continuously exposed to the solar radiation, giving rise to larger temperatures than at the subsolar point.

Note that in the presence of strong Coriolis forces, thermally driven eastward (prograde) flow is generated by poleward temperature gradients and westward (retrograde) flow by equatorward gradients. In our simulations the eastward flow is only found in the solar driven simulations, whereas in runs S6 and S7, where the main heating occurs at polar latitudes, generating equatorward pressure gradients, the flow is primarily westward, as shown in the following.

5.3. Effects of Joule heating

In simulation S6 we introduced latitudinal profiles of Joule heating, as described in Section 4.3. Since these are local time independent and additionally the solar driven local time variations are very small, we will only discuss the diurnally averaged parameters, which are a good representation of the overall atmospheric behavior.

Fig. 6 shows latitude–height panels of temperatures, horizontal winds and H_2 mixing ratios. The simulation is for equinox conditions, so any hemispheric asymmetries are driven by asymmetries in Joule heating (see Section 4.3). Panel (a) shows that temperatures are largest near the poles, a result of the high latitude Joule heating and “trapping” of energy at high latitudes as a result of Coriolis forces. Furthermore, we see the temperature maximum in the polar regions do not lie in the upper thermosphere, as normally expected, but near 10 nbar. At this pressure level, temperatures for 90° N, 0° and 90° S are 1164, 152 and 1197 K, respectively. Near the top of our height range, at 3×10^{-3} nbar the equivalent values are 777, 172 and 815 K, respectively. The sharp latitudinal temperature gradient drives meridional equatorward winds (panel (b)) which peak near 50° latitude with values of around 300 m/s. Note that meridional winds decrease with decreasing altitude, below 1 nbar they are virtually negligible, despite the Joule heating rate per volume being largest near the lower boundary. It is unclear how realistic this behavior is—in our simulations it is linked to our lower boundary condition of vanishing wind velocities. We further see the southern pole to be up to 38 K warmer than the northern one. This agrees with our overall Joule energy input being larger in the south (4.96 TW versus 4.86 TW, see Section 4.3). Correspondingly, there are slight differences between north and south in the dynamics as well. Peak zonal winds in S6 are around 3 km/s.

Fig. 7 shows the same diurnally averaged parameters as Fig. 6, but for simulation S7, where a wave heating profile (dashed–dotted curve in Fig. 3) was applied in addition to the Joule heating (see Section 4.4). We find the overall structures to be very similar. Near the 10 nbar pressure level, temperatures for 90° N, 0° and 90° S are 1253, 365 and 1293 K, respectively, while exospheric values are 894, 407 and 936 K, respectively. When comparing these values to those from S6 (see above), we see equatorial temperatures in S7 increased on average by 224 K and the pole-to-equator exospheric temperature differences reduced from around 624 to 508 K, which

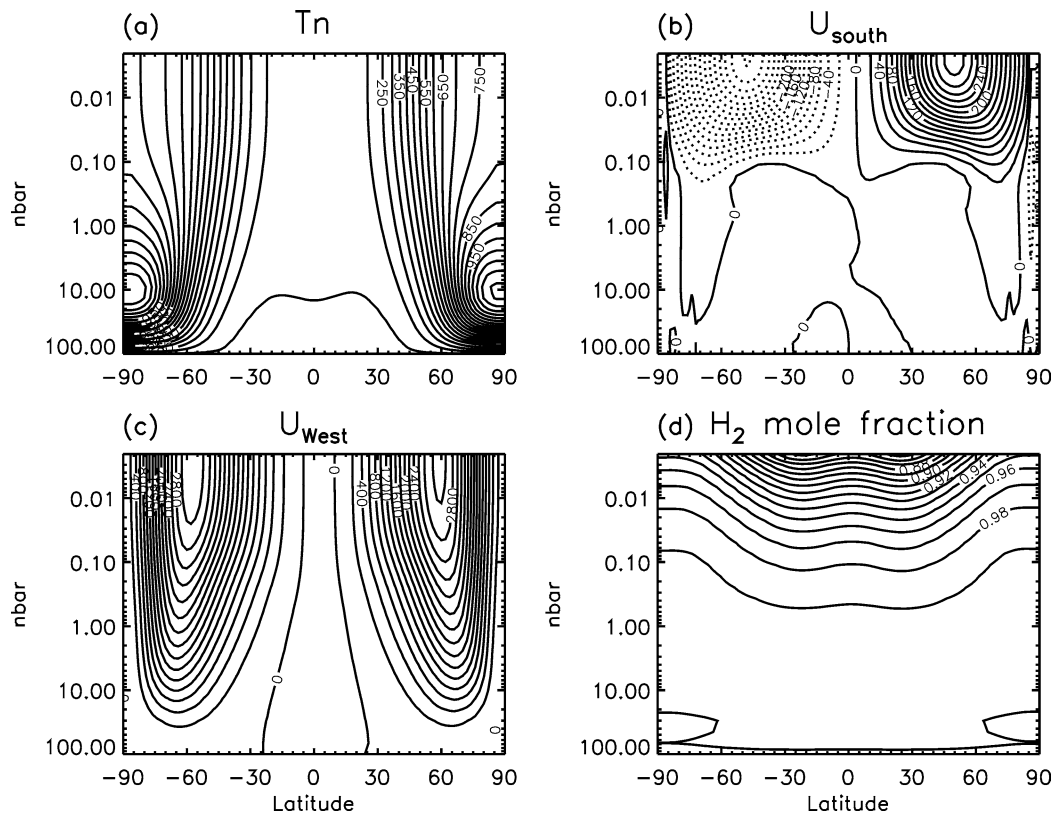


Fig. 6. Diurnally averaged temperatures, horizontal winds and H_2 mixing ratios versus latitude and height for equinox and solar maximum conditions, as calculated by the GCM in simulation S6. U_{South} and U_{West} are meridional and zonal winds, respectively, defined as positive southward and westward.

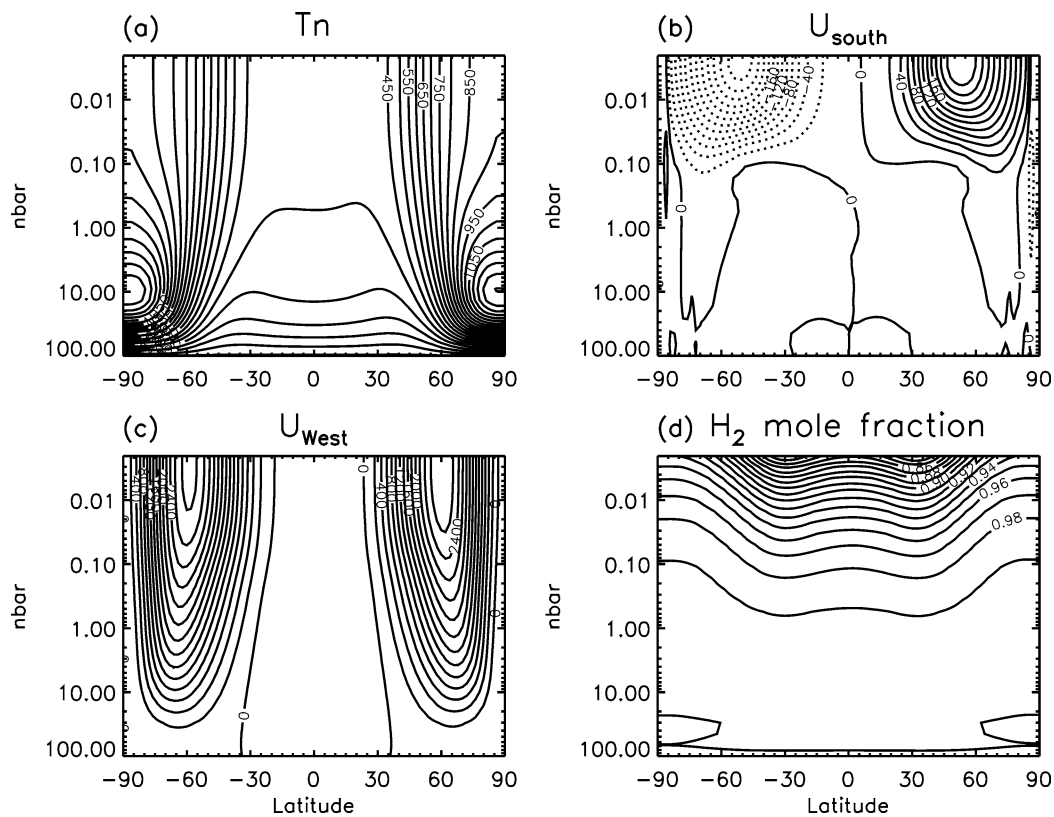


Fig. 7. Same as Fig. 6, but for simulation S7.

in turn affects the dynamics. Meridional and zonal peak wind velocities now reach values of around 230 m/s and 2.7 km/s, respectively.

Fig. 8 shows diurnally averaged meridional accelerations near the 3×10^{-3} nbar pressure level versus latitude from simulation S7. Clearly visible are the strong pressure gradient accelerations (solid line) which point equatorward and are balanced primarily by Coriolis accelerations (dotted), due to the fast rotation rate of the planet. Vertical viscosity (dashed) and curvature (dashed-dotted) also play a role, but of secondary order. The predominance of the pressure–Coriolis balance in the meridional direction explains the meridional and zonal wind component behavior in panels (b) and (c) of Figs. 6 and 7. Despite the meridional pressure gradients being orders of magnitude larger than the zonal ones (which are driven by changes in solar zenith angle only, given that our Joule heating rates are constant with local time and longitude), the meridional winds are deflected by strong Coriolis forces to flow westward instead. Zonal winds peak near 60° latitude in both hemispheres, reaching values of around 3.0 km/s (S6) or 2.7 km/s (S7), reduced in S7 due to the smaller meridional temperature gradients. Zonal winds extend lower down into the thermosphere than meridional winds, at high latitudes essentially to the bottom of our model. Sound speeds in Saturn's thermosphere are $v \approx 2.1$ km/s for $T = 750$ K. The strongest zonal winds in our simulations hence exceed the sound speed.

As mentioned previously (Section 4.3), we ignored the effects of ion drag, which will primarily affect the zonal velocities, but this simplification will hardly affect many of the basic conclusions in our study, such as that about meridional energy transport being inefficient. The observations of H_3^+ velocities by Stallard et al. (2004) found line-of-sight westward auroral ion drifts at $1/3$ the corotation speed, which translates to peak velocities of around 2 km/s in the rotating planet system. The peak of H_3^+ densities, which those measurements sampled, is located in the lower thermosphere, so the observations would suggest the presence of substantial westward ion drag in the lower thermosphere. Depending on the exact ion velocities, they may either accelerate or reduce the neutral westward winds of Figs. 6 and 7 at auroral latitudes and partly affect their latitude structure. At more equatorial latitudes the ions are expected to drift mainly along the magnetic field lines, and hence are likely to decelerate neutral winds there.

Note that the strong thermally driven westward motion by the neutral gases reduces the degree of corotation of the thermosphere with the planet, thereby the collisions between ions and neutrals (which depend on their relative velocities) and hence the amount of Joule heating. In their estimates of the Joule heating rates assumed in our study, Cowley et al. (2004) accounted for this effect by using a scaling parameter, k , the “slippage” of the neutral atmosphere from rigid corotation. The Joule heating rates we assumed in this study assumed perfect corotation of the neutral atmosphere ($k = 0$) and thus represent an upper limit. Joule heating rates would be reduced by a factor of $(1 - k)$ for an atmosphere not in perfect corotation (where $0 < k < 1$). As a result of thermally driven westward winds, the Joule heating rates are hence potentially reduced, lowering

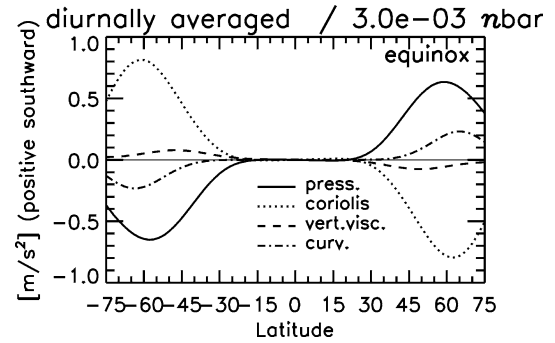


Fig. 8. Diurnally averaged meridional acceleration terms on the 3.0×10^{-3} nbar pressure level in simulation S7. Values are defined as positive southward.

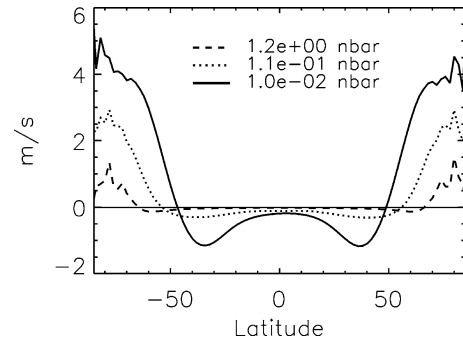


Fig. 9. Latitude plot of diurnally averaged vertical winds on 3 different pressure levels from simulation S7. The 1.2 nbar level roughly corresponds to the main ionospheric peak altitude of 1500 km. Values are defined as positive upward.

the pressure gradients and hence zonal winds, until a balance is reached.

However, Smith et al. (2005b) recently proposed that the case of $k < 1$ does not necessarily lead to a reduction of the energy input from the magnetosphere by a factor of $(1 - k)$. Instead, they propose that the reduced Joule heating is compensated for by increased ion drag, which causes dissipation of kinetic energy via viscous drag and subsequent thermal heating. They propose that a reduction of the neutral atmosphere corotation, despite reducing the component of Joule heating, overall does not affect the total energy input from the magnetosphere into the upper atmosphere, but only its distribution into Joule heating and viscous heating via ion drag. Simulating this self-regulating system of high latitude Joule heating and dynamics will be address in a more self-consistent manner in future studies with our model.

5.4. Vertical velocities and energetics

The horizontal winds discussed in the previous section are accompanied by vertical velocities, which are important both for energetics, causing adiabatic heating and cooling, and for composition. In Fig. 9 we show latitudinal profiles of diurnally averaged vertical velocities on 3 different pressure levels from simulation S7. The 1.2-nbar level roughly corresponds to the main ionospheric peak altitude of 1500 km in photochemical models (Moore et al., 2004). We see that vertical winds can reach 5.0 m/s (upward) at polar latitudes with pronounced

latitudinal structure. Equatorward of around $\pm 50^\circ$ they are negative (downward), reaching peak values of -1.2 m/s.

What drives these vertical velocities? Following Dickinson and Geisler (1968) and Rishbeth and Müller-Wodarg (1999), we may distinguish between two components of vertical wind, the barometric velocity, v_{bar} , and divergence wind, v_{div} , where the total wind, v_z , is the sum of both: $v_z = v_{\text{bar}} + v_{\text{div}}$. While barometric wind is linked to the thermal expansion of the atmosphere, the vertical divergence wind is due to conservation of mass relative to levels of fixed pressure. Diverging (converging) horizontal winds will create an upward (downward) divergence wind. So, the underlying physics driving these two wind components are different. Our calculations distinguish between the two vertical wind components, and we found the total vertical wind velocities, v_z , in Fig. 9 to be primarily divergence winds, driven by the diverging (at high latitudes) and converging (at low latitudes) horizontal winds. This matches well the situation in the Earth's upper atmosphere, where high latitude vertical winds are driven almost entirely by the same processes (Rishbeth and Müller-Wodarg, 1999). For the cases of solar-driven dynamics alone (simulations S1–S5) we found diurnal vertical velocities to be below 0.2 m/s, upward in the sunlit (dayside/summer) hemisphere and downward in the anti-sunward hemisphere. In those simulations, vertical winds were primarily barometric and diurnal averages below 0.02 m/s. This shows that the vertical winds in Fig. 9 are driven primarily by the Joule heating and not by solar heating.

Analysis of the energy equation terms shows most of the energy in Saturn's thermosphere to be lost by downward molecular conduction. However, in runs S6 and S7 vertical winds also play a key role to the energetics. At polar latitudes we find Joule heating to be balanced not only by conduction, but also by cooling through vertical advection and adiabatic processes. Equatorward of $\pm 45^\circ$ the downward vertical velocities cause the opposite, adiabatic heating. Height-integrated adiabatic heating values reach around 15% of the wave heating rates in simulation S7. Vertical and horizontal advection are relatively less important at low latitudes, with rates less than a third those of adiabatic heating. The equatorial downwelling is a direct result of the global pole-to-equator circulation that is driven by the Joule heating. Equatorial adiabatic heating is therefore effectively a means of transporting the energy from the poles to the equator. As already mentioned in Section 5.3, Saturn's fast rotation forces horizontal winds to be primarily zonal and hence less effective than vertical winds in transporting energy equatorward, in agreement with findings by Smith et al. (2005a) and Bougher et al. (2005).

5.5. Wind-driven composition changes

Finally, we investigate the effect of vertical winds on neutral composition in Saturn's thermosphere. Panels (d) of Figs. 6 and 7 show the mole fractions of H_2 from simulations S6 and S7, respectively. In simulations S1–S5 similar profiles (not shown) consisted of essentially horizontal contour lines, with composition varying only vertically, but very little horizontally, due to the small solar-driven velocities (see Section 5.2). Both in

S6 and S7, however, strong horizontal changes appear, with H_2 mixing ratios near the top of our altitude range increasing from equatorial values of 88.2% (S6) and 88.6% (S7) to polar values of 96%. Differences between S6 and S7 are relatively small, the effect being larger in S6 due to the stronger circulation which in S7 is offset by the equatorial heating. In both simulations however there is a noticeable increase in H_2 mixing ratios towards the poles.

This composition change is driven entirely by vertical velocities, given that our auroral forcing currently does not include precipitating particles, which would further contribute towards ionization and hence neutral composition changes. The strong upwelling at high latitudes (see Fig. 9 and Section 5.4) transports gases upward in the atmosphere. The mixing ratios of H_2 , being the relatively heavier gas in Saturn's thermosphere, decrease with altitude due to the separation of constituents above the homopause. When transporting gases upward, therefore, the H_2 mixing ratio locally increases, whereas the opposite happens in regions of downwelling. This transport effect is well known for Earth (Rishbeth and Müller-Wodarg, 1999) and other atmospheres, including Titan's (Müller-Wodarg et al., 2003).

Since H is the lighter gas in Saturn's thermosphere, it behaves opposite to H_2 and the upwelling at auroral latitudes reduces its abundances, while low latitude downwelling enhances them. As shown in Fig. 1, H and H_2 are the principal neutral gases in Saturn's thermosphere at altitudes above the 1-nbar level, so their mixing ratios roughly add up to unity. The abundances of H near the 3.0×10^{-3} -nbar pressure level increase towards the equator, from around 4% near the poles to 12% near the equator, a factor of 3. We find column-integrated H densities to increase by up to 25% at low latitudes with respect to polar values, due to vertical winds. Ben Jaffel et al. (1995) found H densities derived from their reanalyzed Voyager UVS emission data to be enhanced by a factor of 3 with respect to standard models, which are partly based on observations and partly on photochemistry. Amongst the possible explanation for this they ruled out meridional transport of H due to the strong Coriolis forces on Saturn. Our simulations confirm that meridional transport is indeed negligible, but add vertical winds as a possible candidate. We find that wind-induced downward transport could contribute towards this enhancement of H densities. In order to better assess the importance of vertical winds we however need an improved latitude coverage of column integrated H abundances on Saturn.

The H_3^+ ion is known to be an important constituent in the atmosphere of Jupiter, and has also been detected in Saturn's auroral regions (Stallard et al., 1999, 2004). It is generated both by solar EUV ionization and particle precipitation and hence is most abundant in polar regions. As shown recently by Moore et al. (2004) the ratio $\text{H}^+/\text{H}_3^+ \propto \text{Ne}/\text{H}_2$, where Ne is the total electron density, so as H_2 increases, so does H_3^+ . Our calculations show that this could occur due to a change in the background atmosphere, driven by the neutral winds. In the presence of Joule heating, therefore, dynamics lead to an enhancement of H_2 . We will address the effects of this change in neutral composition on H_3^+ densities in future studies.

6. Conclusions

The development of a Saturn Thermosphere–Ionosphere Model (STIM) represents a first attempt at understanding the global morphology of Saturn's thermosphere, including the coupling of energy, dynamics and composition. Keeping in mind the limitations of our calculations, they provide a useful comparison between different bodies in the Solar System and how these react dynamically to external heating. Our simulations reveal important differences between Saturn and the terrestrial planets, as well as Titan. While Saturn's thermosphere is currently too under-constrained by observations to make any reliable predictions ahead of anticipated measurements by the Cassini spacecraft, our calculations help in developing a deeper understanding of Saturn's thermosphere, in particular the interplay of energetics, dynamics and composition.

Overall we find that Joule heating at the rates proposed by Cowley et al. (2004) is insufficient to raise temperatures at low latitudes to observed values. We therefore proposed an additional source of heating, which we called wave heating, to “fill in” the missing energy at low latitudes since Coriolis forces, resulting from the fast rotation of Saturn, prevent effective redistribution of high latitude energy towards lower latitudes. While solar heating is relatively insignificant in the thermosphere of Saturn, in contrast to the terrestrial planets and Titan, its weak periodic forcing may in time help build up oscillations at internal harmonics. Seasonal effects, although weaker than on Earth, Mars and Titan, may contribute towards asymmetries between the hemispheres.

Saturn's real coupled thermosphere–ionosphere system is very complex and our model currently does not include all the physical processes that are likely to occur. This however allows us to better separate the physical processes and assess their individual roles. We ignored ion dynamics and hence the effects of ion–neutral drag both at high latitudes (where neutral winds would be accelerated by fast ions, themselves driven by magnetospheric electric convection fields) and at low latitudes. At low latitudes, the effect would be to slow down the neutral velocities, possibly offsetting some of the strong zonal winds we find in our calculations. This is an extension planned for the near future. Similarly, our method of introducing Joule heating was not self-consistent and hence did not reflect the changes in Joule heating rates which result from changes in the background atmosphere, such as ion densities or dynamics. Another simplification in our simulations was to assume Joule heating to be constant with longitude and local time, while recent UV images of Saturn's aurora showed an auroral oval which is not centered around the magnetic pole (Clarke et al., 2005). Introducing a more realistic auroral oval is likely to affect the high latitude dynamics and also the meridional energy flux. As described in Section 5.3, we find zonal wind velocities that exceed the sound speed. This result needs to be treated with caution, given that one implicit assumption of the Navier–Stokes equations that we use in our model is subsonic flow. However, the result shows that the pressure gradients driven by Joule heating can drive considerable winds close to the sound speed.

It is well known for Earth, Mars and Venus that the upper atmosphere is strongly affected by the lower atmosphere regions, through a general background circulation being present (super-rotation on Venus) and/or the presence of upward propagating waves, which deposit momentum and energy in the upper atmosphere. On all terrestrial planets the thermospheric behavior cannot be understood without taking these into account. The same may be true for Titan, as shown in calculations by Müller-Wodarg et al. (2000), and our discussion of energetics on Jupiter and Saturn (Section 2) has already suggested that the same may be true on the Gas Giants. The presence of strong zonal winds in the troposphere of Saturn is well known, with some evidence of their presence reaching into the stratosphere and mesosphere as well (Hubbard et al., 1997). They may hence be present also at the bottom of the thermosphere, which would affect dynamics there. In calculations of Titan's thermosphere, Müller-Wodarg et al. (2000) included zonal jets at the bottom boundary and found them to super-pose, essentially linearly, onto thermospheric winds. We have not included this in our current calculations, but will do so once more constraints are available for zonal winds near the lower range of our model, and also on the other energy sources considered in our study.

One key aim of studying Saturn's global thermosphere and its dynamics is to improve our understanding of Saturn's ionosphere as well. The ionosphere is strongly coupled energetically, chemically and dynamically to the thermosphere. To date, the vertical structure of Saturn's ionosphere, as observed by the Pioneer 11 and Voyager spacecraft (Kliore et al., 1980; Lindal et al., 1985), has not yet been reproduced successfully by 1-D photochemical ionosphere models, which generally overestimate peak electron densities and place the plasma peak altitude too low. To rectify these discrepancies, Majeed and McConnell (1996) proposed, amongst other effects, substantial vertical plasma drifts to improve the peak density height calculations. To date, inclusion of these drifts in the 1-D ionosphere calculations has been empirical since no information on thermospheric dynamics, which could drive parts of these drifts by pushing ionization along magnetic field lines, was available. In fact, the strong equatorward meridional winds we found in our calculations (see Figs. 6 and 7) could support such strong vertical plasma drifts. The Saturn ionosphere model by Moore et al. (2004) is already fully coupled chemically to our GCM, and the two codes are currently also being coupled dynamically to allow more accurate ionospheric studies of Saturn and elucidation of the role of dynamical coupling between the neutrals and ions on Saturn. This will also be important to address the physics of magnetospheric driving in a self-consistent manner.

Acknowledgments

The work of I.M.W. is funded by a British Royal Society fellowship and by NASA Grant NAG5-12095. At Boston University, this work was funded by a grant from NASA's Planetary Atmospheres program, and by seed research funds at the Center for Space Physics. We are very grateful to Luke Moore and John Clarke for their important contributions to this work. Further-

more, we wish to thank Jack McConnell and Stan Cowley for their thorough reviews of the manuscript and many very helpful suggestions.

Appendix A

General Circulation Models (GCMs) are created with the aim of simulating the global coupling of all processes in an atmospheric system. These are embodied in coupled non-linear Navier–Stokes equations of momentum, energy and continuity, which assume that atmospheric gases behave like fluids. Therefore, GCMs are physical models, which make no assumptions except for boundary conditions, molecular gas parameters and external inputs such as solar EUV flux or other heating, and calculate in a physically self-consistent manner the time-dependent response of atmospheric gases to such external inputs. Realistically, and for reasons of computational efficiency, some processes are simplified, as long as this introduces no important scientific limitation. Wherever such approximations are made, we will point them out in the following.

The Saturn Thermosphere GCM solves numerically, by explicit time integration, the coupled 3-dimensional Navier–Stokes equations of momentum, energy and continuity above 100 nbar (800 km). The two horizontal components of the momentum equation in spherical pressure coordinates are given by

$$\begin{aligned} \frac{\partial u_\theta}{\partial t} = & - \left(u_\theta \frac{1}{a} \frac{\partial u_\theta}{\partial \theta} + u_\varphi \frac{1}{a \sin \theta} \frac{\partial u_\theta}{\partial \varphi} + w \frac{\partial u_\theta}{\partial p} \right) \\ & + \left(\frac{w u_\theta}{a \rho g} + \frac{u_\varphi^2}{a \tan \theta} \right) - \frac{g}{a} \frac{\partial h_p}{\partial \theta} + 2\Omega u_\varphi \cos \theta \\ & + \frac{1}{\rho} \left(\mu \nabla_p^2 u_\theta + \frac{1}{a^2} \frac{\partial \mu}{\partial \theta} \frac{\partial u_\theta}{\partial \theta} + \frac{1}{a^2 \sin^2 \theta} \frac{\partial \mu}{\partial \varphi} \frac{\partial u_\theta}{\partial \varphi} \right) \\ & + \frac{g}{a^2} \frac{\partial}{\partial p} \left(a^2 \mu \rho g \frac{\partial u_\theta}{\partial p} \right), \end{aligned} \quad (\text{A.1})$$

$$\begin{aligned} \frac{\partial u_\varphi}{\partial t} = & - \left(u_\theta \frac{1}{a} \frac{\partial u_\varphi}{\partial \theta} + u_\varphi \frac{1}{a \sin \theta} \frac{\partial u_\varphi}{\partial \varphi} + w \frac{\partial u_\varphi}{\partial p} \right) \\ & - \left(\frac{-w u_\varphi}{a \rho g} + \frac{u_\theta u_\varphi}{a \tan \theta} \right) - \frac{g}{a \sin \theta} \frac{\partial h_p}{\partial \varphi} - 2\Omega u_\theta \cos \theta \\ & + \frac{1}{\rho} \left(\mu \nabla_p^2 u_\varphi + \frac{1}{a^2} \frac{\partial \mu}{\partial \theta} \frac{\partial u_\varphi}{\partial \theta} + \frac{1}{a^2 \sin^2 \theta} \frac{\partial \mu}{\partial \varphi} \frac{\partial u_\varphi}{\partial \varphi} \right) \\ & + \frac{g}{a^2} \frac{\partial}{\partial p} \left(a^2 \mu \rho g \frac{\partial u_\varphi}{\partial p} \right). \end{aligned} \quad (\text{A.2})$$

Here u_θ and u_φ are the neutral wind components, defined as positive southward and eastward, respectively; a is the distance to the center of the planet, θ is colatitude, φ is the longitude, h_p is the height of the pressure level and t is time. Furthermore, g is the (height-dependent) gravitational acceleration, ρ the mass density, p the pressure, Ω is Saturn's rotation period (with $\Omega = 1.64 \times 10^{-4} \text{ s}^{-1}$, corresponding to 10.6 h) and μ is the coefficient of viscosity. We calculate viscosities using the same technique and coefficients as Achilleos et al. (1998). w is the vertical wind in the pressure frame, defined as $w = dp/dt$.

The total vertical velocity in the height frame u_z is obtained by adding the velocity of the pressure level itself (barometric velocity) to the velocity relative to the pressure level (divergence velocity), $-1/(\rho g)w$: $u_z = (\partial h_p / \partial t) - 1/(\rho g)w$.

$\vec{\nabla}_p$ is the 2-dimensional gradient operator on a level of fixed pressure. For its square we use the expression

$$\nabla_p^2 = \frac{1}{a^2} \frac{\partial^2}{\partial \theta^2} + \frac{\cos \theta}{a^2 \sin \theta} \frac{\partial}{\partial \theta} + \frac{1}{a^2 \sin^2 \theta} \frac{\partial^2}{\partial \varphi^2}. \quad (\text{A.3})$$

In the vertical direction, the pressure gradient and gravity acceleration dominate other terms by several orders of magnitude and an accurate numerical calculation of the vertical velocity w by solving the vertical component of the momentum equation is numerically difficult. Vertical winds are therefore calculated using the continuity equation, which in the pressure coordinate system reduces to the simple form of

$$\frac{1}{a \sin \theta} \frac{\partial}{\partial \theta} u_\theta \sin \theta + \frac{1}{a \sin \theta} \frac{\partial u_\varphi}{\partial \varphi} + \frac{\partial w}{\partial p} = 0. \quad (\text{A.4})$$

Physically, the equation expresses that any divergence in the horizontal velocity field must be balanced by vertical wind in order to conserve mass. To calculate w we use the technique described by Müller-Wodarg et al. (2000). As boundary conditions for the momentum equation we assume fixed wind velocities (of zero) at the bottom and vanishing vertical gradients of wind components at the top level. In our expression for gravity we do not include the centrifugal component due to Saturn's strong rotation. While not strictly correct, it ensures that our calculations are consistent with the requirements of our coordinate system that gravity always point towards a common centre of the body. The issue matters only when mapping pressure levels to altitudes, which we have not attempted in this paper, but it does not affect to first order the calculations on pressure levels themselves.

The energy balance is given by the sum of the internal and external energy sources and sinks. In a spherical pressure coordinate system it may be expressed by the relation

$$\begin{aligned} \frac{\partial \epsilon}{\partial t} + \vec{U}_p \cdot \vec{\nabla}_p (\epsilon + g h_p) + w \frac{\partial (\epsilon + g h_p)}{\partial p} \\ = Q_{\text{EUV}} + Q_{\text{Joule}} + Q_{\text{wave}} + Q_{\text{IR}} \\ + \frac{g}{a^2} \frac{\partial}{\partial p} \left(a^2 \frac{(K_m + K_\tau)}{H} p \frac{\partial T}{\partial p} \right) + \frac{1}{\rho} (K_m + K_\tau) \vec{\nabla}_p^2 T \\ + g \frac{\partial}{\partial p} \left(u_\theta \mu \frac{\partial u_\theta}{\partial p} + u_\varphi \mu \frac{\partial u_\varphi}{\partial p} \right). \end{aligned} \quad (\text{A.5})$$

Here ϵ is the sum of internal and kinetic energies per unit mass, defined as $\epsilon = c_p T + 0.5(u_\theta^2 + u_\varphi^2)$, and T is gas temperature. With $g h_p$ representing the potential energy of the gas at height h_p , the term $\epsilon + g h_p$ is thus its enthalpy. Coefficients of molecular conduction (K_m) are equivalent to those of Achilleos et al. (1998), with turbulent conduction currently being set to zero.

Q_{EUV} is heating due to solar EUV and FUV radiation which is absorbed by H_2 , H and He at wavelengths between 7.5 and around 103.2 nm, in particular the He II line (30.38 nm). We derive solar EUV heating rates by explicit calculation of photon

absorption along ray paths through the atmosphere, assuming a heating efficiency of 50% for all constituents and wavelengths. Another implicit assumption in these heating rate calculations is that thermal energy is released where the photons are absorbed. While this poses no serious limitation for our current purpose, we will in the future replace this approximation with explicit calculations of chemical heating rates. We use absorption cross-sections consistent with those of Moses et al. (2000a) and solar EUV fluxes from the SOLAR2000 model (Tobiska et al., 2000; Tobiska, 2004). Another option in the model is to include effects of ring shadowing, but we have ignored it in this study. Radiative cooling Q_{IR} in Saturn's thermosphere occurs primarily near and below the homopause and can be ignored for our purpose. Q_{wave} and Q_{Joule} are wave and Joule heating, described in Sections 4.2 and 4.3. As boundary conditions for the energy equation we assume fixed temperature (of 143 K) at the bottom and zero vertical temperature gradients at the top.

In addition, our model allows for the dynamical redistribution of individual gases by explicitly calculating their transport by winds and molecular and eddy diffusion. While transport by winds is treated both horizontally and vertically, we calculate molecular and eddy diffusion only in the vertical direction, since vertical gradients are much larger than horizontal gradients, making horizontal diffusion negligible. The molecular diffusion velocities are given by

$$\frac{\partial Y_i}{\partial z} - \left(1 - \frac{m_i}{m} - \frac{H}{m} \frac{\partial m}{\partial z}\right) \frac{Y_i}{H} = - \sum_{j \neq i} \frac{m Y_i Y_j}{m_j D_{ij}} (w_i^D - w_j^D), \quad (\text{A.6})$$

where $Y_i = \rho_i / \rho$ and m_i are the mass fraction and molecular mass of the i th constituent, m is the mean molecular mass of the atmosphere, H is the pressure scale height, D_{ij} is the binary diffusion coefficient, and w_i^D is the vertical diffusion velocity of the i th constituent (Chapman and Cowling, 1970). Molecular constituents are also subject to eddy diffusion, which we calculate with

$$w_i^K = -K \frac{\partial \ln(Y_i)}{\partial z}, \quad (\text{A.7})$$

where K is the eddy diffusion coefficient. Here, K represents mixing due to small-scale motions not resolved by the model. The diffusion velocities are then used in the continuity equation to calculate the time development of mass fractions. The continuity equation for the i th constituent is given in spherical pressure coordinates by

$$\begin{aligned} \frac{\partial Y_i}{\partial t} + u_\theta \frac{1}{a} \frac{\partial Y_i}{\partial \theta} + u_\varphi \frac{1}{a \sin \theta} \frac{\partial Y_i}{\partial \varphi} + w \frac{\partial Y_i}{\partial p} \\ = \frac{g}{a^2} \frac{\partial}{\partial p} (a^2 \rho Y_i (w_i^D + w_i^K)) + J_i, \end{aligned} \quad (\text{A.8})$$

where J_i is the net chemical source rate (Dickinson and Ridley, 1975). The velocities u_θ , u_φ and w represent the mean velocity of the atmosphere, defined as the average of the velocities of individual constituents, weighted by their mass densities.

Our GCM calculations include the three thermally active species in Saturn's thermosphere, H_2 , H and He . We also include a basic scheme of ion-neutral chemistry, as described

by Moore et al. (2004) and Moses and Bass (2000). While we generate a global photochemical ionosphere in the model, we currently do not allow for dynamics of the ions, a development step we will undertake in the near future.

Molecular diffusion coefficients are calculated using the standard expression $D_{ij} = A_{ij} T^{s_{ij}} / n_j$ (cm^2/s), where n_j is the major gas density and A_{ij} for pairs H_2 - H , H_2 - He and He - H are, in cgs units, given by 8.19×10^{17} , 6.45×10^{17} and 8.84×10^{17} (Banks and Kockarts, 1973; Bernhardt, 1979). For the same gas pairs, values for s_{ij} are 0.728, 0.716 and 0.706, respectively. We ignore self-diffusion ($A_{ii} = A_{jj} = 0$) and assume $A_{ij} = A_{ji}$.

We adopt an eddy coefficient for small-scale motions of $K = 1 \times 10^7 \text{ cm}^2 \text{ s}^{-1}$, assumed constant with altitude. This places the homopause near the 70-nbar level, or around 850 km altitude, allowing us to currently neglect the complex photochemistry near and below the homopause.

Our present calculations use spatial resolutions of between 2° - 6° latitude by 10° longitude by 0.25 scale heights vertically and integrate with a 1-40 s time step. Each simulation is run to steady state for 400 Saturn rotations.

References

- Achilleos, N., Miller, S., Tennyson, J., Aylward, A.D., Müller-Wodarg, I.C.F., Rees, D., 1998. JIM: A time-dependent, three-dimensional model of Jupiter's thermosphere and ionosphere. *J. Geophys. Res.* 103, 20089-20112.
- Banks, P.M., Kockarts, G., 1973. *Aeronomy*. Academic Press, New York.
- Ben Jaffel, L., Prangé, R., Sandel, B.R., Yelle, R.V., Emerich, C., Feng, D., Hall, D.T., 1995. New analysis of the Voyager UVS H Lyman- α emission of Saturn. *Icarus* 113, 91-102.
- Bernhardt, P.A., 1979. Three-dimensional, time-dependent modeling of neutral gas diffusion in a nonuniform, chemically reactive atmosphere. *J. Geophys. Res.* 84, 793-802.
- Bhardwaj, A., Branduardi-Raymont, G., Elsner, R.F., Gladstone, G.R., Ramsay, G., Rodriguez, P., Soria, R., Waite Jr., J.H., Cravens, T.E., 2004. Solar control on Jupiter's equatorial X-ray emissions: 26-29 November 2003 XMM-Newton observation. *Geophys. Res. Lett.* 32, doi:10.1029/2004GL021497. L03S08.
- Bhardwaj, A., Elsner, R.F., Waite Jr., J.H., Gladstone, G.R., Cravens, T.E., Ford, P.G., 2005. Chandra observation of an X-ray flare at Saturn: Evidence of direct solar control on Saturn's disk X-ray emissions. *Astrophys. J.* 624, L121-L124.
- Bougher, S.W., Engel, S., Roble, R.G., Foster, B., 1999. Comparative terrestrial planet thermospheres. 2. Solar cycle variation of global structure and winds at equinox. *J. Geophys. Res.* 104, 16591-16611.
- Bougher, S.W., Engel, S., Roble, R.G., Foster, B., 2000. Comparative terrestrial planet thermospheres. 3. Solar cycle variation of global structure and winds at solstices. *J. Geophys. Res.* 105, 17669-17692.
- Bougher, S.W., Roble, R.G., Fuller-Rowell, T.J., 2002. Simulations of the upper atmospheres of the terrestrial planets. In: Mendillo, M., Nagy, A., Waite, H. (Eds.), *Comparative Atmospheres in the Solar System*. Am. Geophys. Union, Washington, DC, pp. 261-288.
- Bougher, S.W., Waite, J.H., Majeed, T., Gladstone, G.R., 2005. Jupiter Thermospheric General Circulation Model (JTGCM): Global structure and dynamics driven by auroral and Joule heating. *J. Geophys. Res.* 110, doi:10.1029/2003JE002230. E04008.
- Chapman, S., Cowling, T.G., 1970. *The Mathematical Theory of Non-Uniform Gases*. Cambridge Univ. Press, Cambridge, UK.
- Clarke, J.T., Gérard, J.-C., Grodent, D., Wannawichian, S., Gustin, J., Connerney, J., Crary, F., Dougherty, M., Kurth, W., Cowley, S.W.H., Bunce, E.J., Hill, T., Kim, J., 2005. Morphological differences between Saturn's ultraviolet aurorae and those of Earth and Jupiter. *Nature* 433, 717-719.

- Cowley, S.W.H., Bunce, E.J., O'Rourke, J.M., 2004. A simple quantitative model of plasma flows and currents in Saturn's polar ionosphere. *J. Geophys. Res.* 109, doi:10.1029/2003JA010375. A05212.
- Davis Jr., L., Smith, E.J., 1990. A model of Saturn's magnetic field based on all available data. *J. Geophys. Res.* 95, 15257–15261.
- Dickinson, R.E., Geisler, J.E., 1968. Vertical motion field in the middle thermosphere from satellite drag densities. *Mon. Weather Rev.* 96, 606–616.
- Dickinson, R.E., Ridley, E.C., 1975. A numerical model for the dynamics and composition of the venusian thermosphere. *J. Atmos. Sci.* 32, 1219–1231.
- Festou, M.C., Atreya, S.K., 1982. Voyager ultraviolet stellar occultation measurements of the composition and thermal profiles of the saturnian upper atmosphere. *Geophys. Res. Lett.* 9, 1147–1150.
- French, R.G., Gierasch, P.J., 1974. Waves in the jovian upper atmosphere. *J. Atmos. Sci.* 31, 1707–1712.
- Fuller-Rowell, T.J., Rees, D., Quegan, S., Moffett, R.J., Codrescu, M.V., Millward, G.H., 1996. A coupled thermosphere–ionosphere model (CTIM). In: Schunk, R.W. (Ed.), *Handbook of Ionospheric Models*. Scientific Committee on Solar-Terrestrial Physics, pp. 217–238.
- Hubbard, W.B., and 27 colleagues, 1997. Structure of Saturn's mesosphere from the 28 Sgr occultations. *Icarus* 130, 404–425.
- Hunten, D., Dessler, A.J., 1977. Soft electrons as a possible heat source for Jupiter's thermosphere. *Planet. Space Sci.* 25, 817–821.
- Kliore, A., Patel, I.R., Lindal, G.F., Sweetnam, D.N., Hotz, H.B., Waite, J.H., McDonough, T.R., 1980. Structure of the ionosphere and atmosphere of Saturn from Pioneer 11 radio occultation. *J. Geophys. Res.* 85, 5857–5870.
- Lindal, G.F., 1992. The atmosphere of Neptune: An analysis of radio occultation data acquired with Voyager 2. *Astron. J.* 103, 967–982.
- Lindal, G.F., Sweetnam, D.N., Eshleman, V.R., 1985. The atmosphere of Saturn—An analysis of the Voyager radio occultation measurements. *Astron. J.* 90, 1136–1146.
- Majeed, T., McConnell, J.C., 1996. Voyager electron density measurements on Saturn: Analysis with a time-dependent ionospheric model. *J. Geophys. Res.* 101, 7589–7598.
- Marten, A., de Bergh, C., Owen, T., Gautier, D., Maillard, J., Drossart, P., Lutz, B.L., Orton, G., 1994. Four-micron high-resolution spectra of Jupiter in the North Equatorial Belt: H_3^+ emission and $^{12}C/^{13}C$ ratio. *Planet. Space Sci.* 42, 391–399.
- Matcheva, K.I., Strobel, D.F., 1999. Heating of Jupiter's thermosphere by dissipation of gravity waves due to molecular viscosity and heat conduction. *Icarus* 140, 328–340.
- Maurellis, A.N., Cravens, T.E., Gladstone, G.R., Waite, J.H., Acton, L.W., 2000. Jovian X-ray emission from solar X-ray scattering. *Geophys. Res. Lett.* 27 (9), 1339–1342.
- Mendillo, M., Moore, L., Clarke, J., Müller-Wodarg, I.C.F., Kurth, W., 2005. Effects of ring shadowing on the detection of electrostatic discharges at Saturn. *Geophys. Res. Lett.* 32, doi:10.1029/2004GL021934. L05107.
- Millward, G.H., Miller, S., Aylward, A.D., Müller-Wodarg, I.C.F., Achilleos, N., 2002. Thermospheric General Circulation Models for the giant planets: The Jupiter case. In: Mendillo, M., Nagy, A., Waite, H. (Eds.), *Comparative Atmospheres in the Solar System*. Am. Geophys. Union, Washington, DC, pp. 289–298.
- Moore, L., Mendillo, M., 2005. Ionospheric contribution to Saturn's inner plasmasphere. *J. Geophys. Res.* 110, doi:10.1029/2004JA010889. A05310.
- Moore, L., Mendillo, M., Müller-Wodarg, I.C.F., Murr, D., 2004. Modeling of global variations and ring shadowing in Saturn's ionosphere. *Icarus* 172, 503–520.
- Moses, J.I., Bass, S.F., 2000. The effects of external material on the chemistry and structure of Saturn's ionosphere. *J. Geophys. Res.* 105, 7013–7052.
- Moses, J.I., Lellouch, E., Bézard, B., Gladstone, G.R., Feuchtgruber, H., Allen, M., 2000a. Photochemistry of Saturn's atmosphere. II. Effects of an influx of external oxygen. *Icarus* 145, 166–202.
- Moses, J.I., Bézard, B., Lellouch, E., Gladstone, G.R., Feuchtgruber, H., Allen, M., 2000b. Photochemistry of Saturn's atmosphere. I. Hydrocarbon chemistry and comparisons with ISO observations. *Icarus* 143, 244–298.
- Müller-Wodarg, I.C.F., 2002. The application of General Circulation Models to the atmospheres of terrestrial-type moons of the giant planets. In: Mendillo, M., Nagy, A., Waite, H. (Eds.), *Comparative Atmospheres in the Solar System*. Am. Geophys. Union, Washington, DC, pp. 307–318.
- Müller-Wodarg, I.C.F., Yelle, R.V., Mendillo, M., Young, L.A., Aylward, A.D., 2000. The thermosphere of Titan simulated by a global three-dimensional time-dependent model. *J. Geophys. Res.* 105, 20833–20856.
- Müller-Wodarg, I.C.F., Yelle, R.V., Mendillo, M., Aylward, A.D., 2003. On the global distribution of neutral gases in Titan's upper atmosphere and its effect on the thermal structure. *J. Geophys. Res.* 108, doi:10.1029/2003JA010054.
- Ollivier, J.L., Dobrijević, M., Parisot, J.P., 2000. New photochemical model of Saturn's atmosphere. *Planet. Space Sci.* 48, 699–716.
- Rishbeth, H., Müller-Wodarg, I.C.F., 1999. Vertical circulation and thermospheric composition: A modeling study. *Ann. Geophys.* 17, 794–805.
- Roble, R.G., Ridley, E.C., Richmond, A.D., Dickinson, R.E., 1988. A coupled thermosphere/ionosphere general circulation model. *Geophys. Res. Lett.* 15, 1325–1328.
- Schubert, G., Hickey, M.P., Walterscheid, R.L., 2003. Heating of Jupiter's thermosphere by the dissipation of upward propagating acoustic waves. *Icarus* 163, 398–413.
- Smith, G.R., Hunten, D.M., 1990. Study of planetary atmospheres by absorptive occultations. *Rev. Geophys.* 28, 117–143.
- Smith, G.R., Shemansky, D.E., Holberg, J.B., Broadfoot, A.L., Sandel, B.R., McConnell, J.C., 1983. Saturn's upper atmosphere from the Voyager 2 EUV solar and stellar occultations. *J. Geophys. Res.* 88, 8667–8678.
- Smith, C.G.A., Aylward, A.D., Miller, S., Müller-Wodarg, I.C.F., 2005a. Polar heating in the Saturn's thermosphere. *Ann. Geophys.* In press.
- Smith, C.G.A., Miller, S., Aylward, A.D., 2005b. Magnetospheric energy inputs into the upper atmospheres of the giant planets. *Ann. Geophys.* 23, 1943–1947.
- Stallard, T., Miller, S., Ballester, G.E., Rego, D., Joseph, R., Trafton, L., 1999. The H_3^+ latitudinal profile of Saturn. *Astrophys. J.* 521, L149–L152.
- Stallard, T., Miller, S., Trafton, L.M., Geballe, T.R., Joseph, R.D., 2004. Ion winds in Saturn's southern auroral/polar region. *Icarus* 167, 204–211.
- Strobel, D.F., Smith, G.R., 1973. On the temperature of the jovian thermosphere. *J. Atmos. Sci.* 30, 718–725.
- Tobiska, W.K., 2004. SOLAR2000 irradiances for climate change research, aeronomy and space system engineering. *Adv. Space Res.* 34, 1736–1746.
- Tobiska, W.K., Woods, T., Eparvier, F., Viereck, R., Floyd, L., Bouwer, D., Rottman, G., White, O.R., 2000. The SOLAR2000 empirical solar irradiance model and forecast tool. *J. Atmos. Solar Terr. Phys.* 62, 1233–1250.
- Waite Jr., J.H., Cravens, T.E., Kozyra, J.U., Nagy, A.F., Atreya, S.K., Chen, R.H., 1983. Electron precipitation and related aeronomy of the jovian thermosphere and ionosphere. *J. Geophys. Res.* 88, 6143–6163.
- Waite Jr., J.H., Gladstone, G.R., Lewis, W.S., Drossart, P., Cravens, T.E., Maurellis, A.N., Mauk, B.H., Miller, S., 1997. Equatorial X-ray emissions: Implications for Jupiter's high exospheric temperatures. *Science* 276, 104–108.
- Yelle, R.V., Miller, S., 2004. Jupiter's thermosphere and ionosphere. In: Bagenal, F., McKinnon, W., Dowling, T. (Eds.), *Jupiter: Planet Satellites and Magnetosphere*. Cambridge Univ. Press, Cambridge, pp. 185–218.
- Yelle, R.V., Young, L.A., Vervack, R.J., Young, R., Pfister, L., Sandel, B.R., 1996. Structure of Jupiter's upper atmosphere: Predictions for Galileo. *J. Geophys. Res.* 101, 2149–2161.
- Young, L.A., Yelle, R.V., Young, R., Sieff, A., Kirk, D.B., 1997. Gravity waves in Jupiter's thermosphere. *Science* 276, 108–111.